Supporting Information

Operando Multimodal Electron Microscopy of Perovskite Nano-LEDs - Nanoscale Degradation and Recovery Behaviour

Linh Lan Nguyen[1], Luiz H. G. Tizei[2], Saskia Fiedler[3], Yves Auad[2], Ingrid Marie Andersen[1], Chris Boothroyd[4], Laura Bocher[2], Martial Duchamp[1], Albert Polman*[3], Yeng Ming Lam*[1,4]*

[1] School of Materials Science and Engineering, Nanyang Technological University, 50 Nanyang Ave, Singapore 639798

[2] Université Paris-Saclay, CNRS, Laboratoire de Physique des Solides, 91405 Orsay, France

[3] Department of Sustainable Energy Materials, NWO-Institute AMOLF, Science Park 104, 1098 XG Amsterdam, Netherlands

[4] Facility for Analysis Characterisation Testing and Simulation, Nanyang Technological University, Singapore 639798

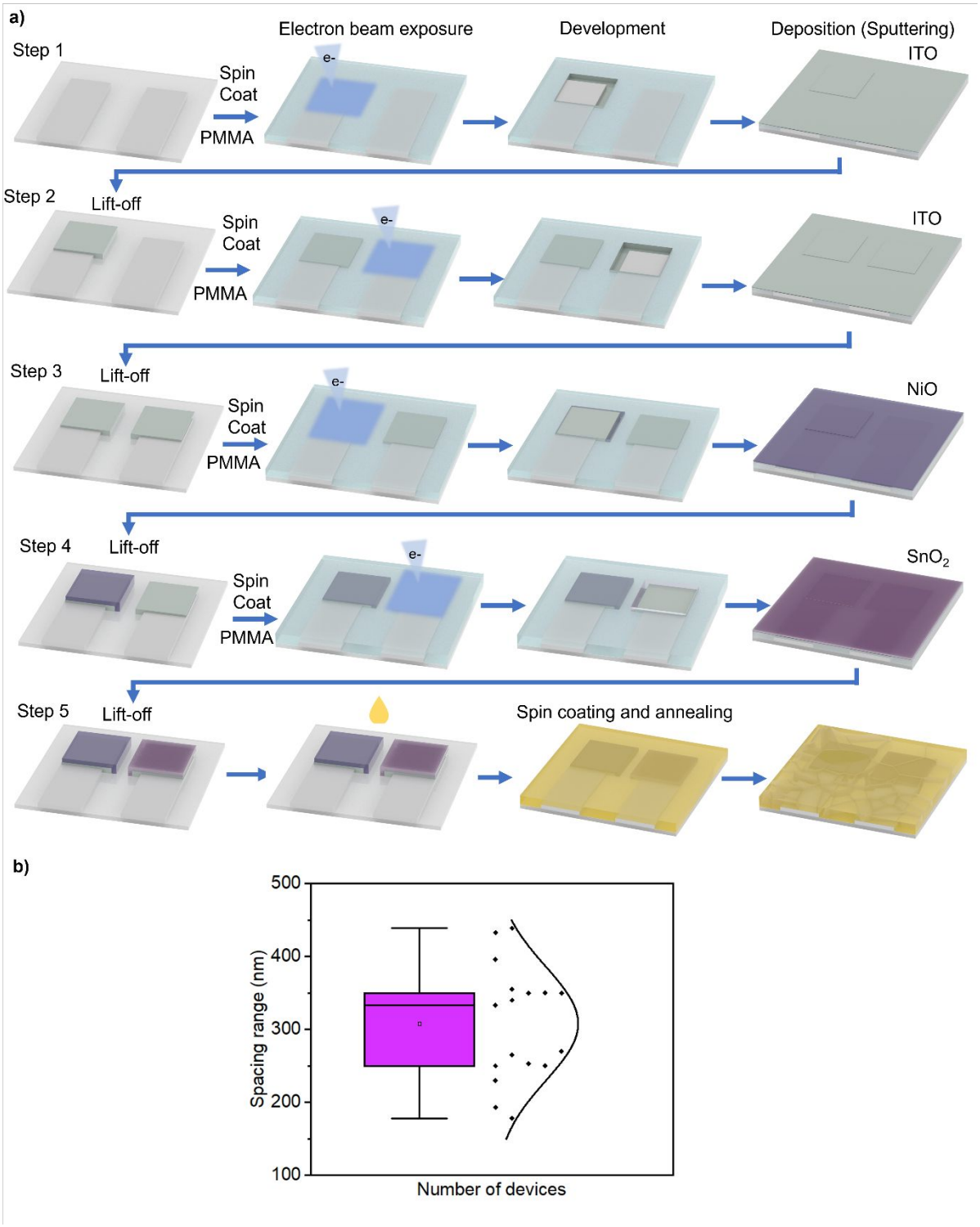

Supplementary Figure 1: Device fabrication. (a) Schematic representation of the 5 fabrication steps for making a full nano LED on a MEMS chip. (b) Box plot of the spacings measured from multiple nano-LEDs devices fabricated by the fabrication process in (a).

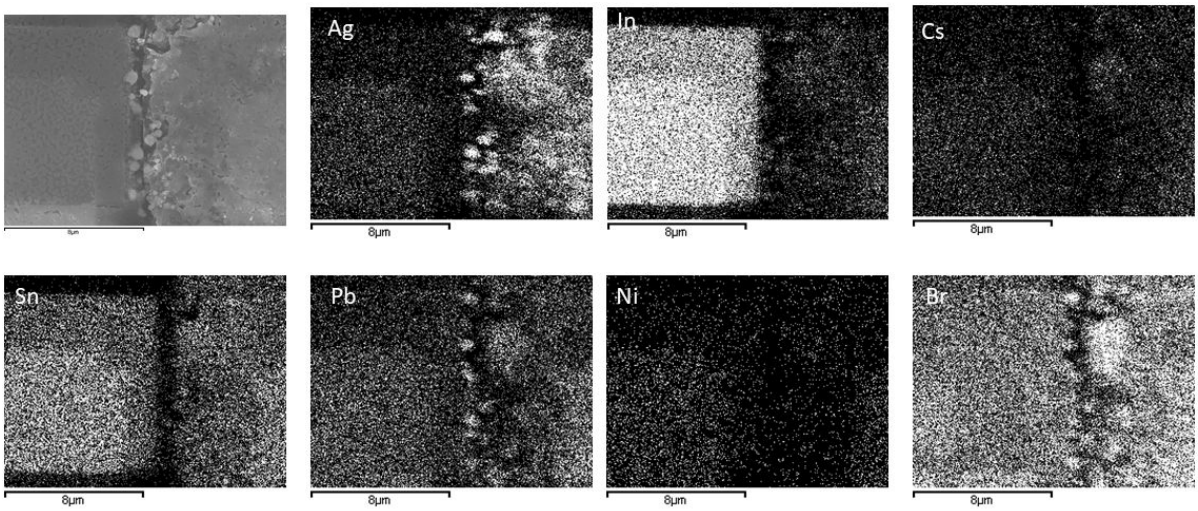

Supplementary Figure 2: EDX analysis of the degraded ITO/NiO/$CsPbBr_3$/SnO_2/Ag device after biasing for 10 minutes with a voltage ramp from 10 V to 20 V. Secondary electron image (top left) together with elemental maps of Ag, In, Cs, Sn, Pb, Ni and Br.

Dose Testing

TEM

The electron dose threshold that causes electron beam damage can vary depending on the dose rate used in a particular imaging mode and the perovskite thickness. [1-3] 50-60 nm large $CsPbBr_3$ nanobricks were reported to have improved electron beam stability compared to 3 nm $CsPbBr_3$ nanocubes due to the reduced number of bromine vacancies present in the thicker perovskites.[1] $CsPbBr_3$ thin films prepared by one-step spin coating in this study possess a thickness in the range of 60 to 100 nm,[4] which is more closely matched with the 50-60 nm nanobricks that exhibit improved electron beam stability in the study by Diao *et al.*[1] In their study, $CsPbBr_3$ nanobricks remain stable under a total dose of 9000 $eÅ^{-2}$ when a dose rate < 500 $eÅ^{-2}s^{-1}$ was utilized in TEM mode.[1] Additionally, they also noted that increasing the dose rate to 1250 $eÅ^{-2}s^{-1}$ significantly reduced the electron dose threshold before desorption of Br occurred causing material loss.[1] Based on Diao's and other studies of $CsPbBr_3$ nanocubes under electron beam exposure,[1,3] the electron dosage was kept below 9000 $eÅ^{-2}$ for the *in-situ* TEM experiments, using a dose rate of 50 $eÅ^{-2}s^{-1}$ (Supplementary Figure 3). The tests in Supplementary Figure 3 confirmed the absence of Pb nanoparticle formation and material loss.

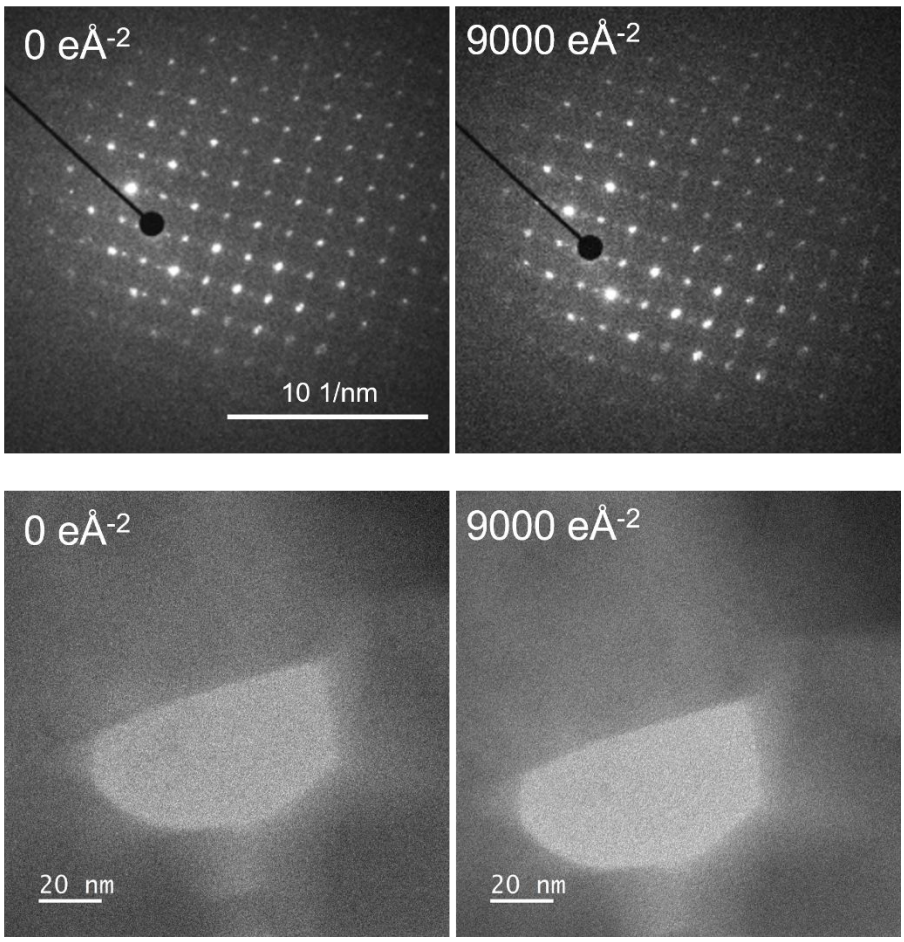

Supplementary Figure 3: Dose study of $CsPbBr_3$ deposited film. Continuous electron beam exposure on the deposited film for 3 minutes under dose rate of 50 $eÅ^{-2}s^{-1}$ did not result in formation of high contrast nanoparticles or any structural transformations characteristic of beam damage.

STEM

For STEM imaging, which typically has a high dose rate, the electron damage dose threshold is usually lower than for TEM imaging. For a 3 nm $CsPbBr_3$ film, the desorption of Br resulting in formation of Pb nanoparticles was already observed at 400 $eÅ^{-2}$ using a dose rate in the range of 8.5×10^5 to 10^8 $eÅ^{-2}s^{-1}$ in a study by Dang *et al.*[3] Notably, the heating effect induced by the electron beam was reported to be negligible at a dose rate of 8.5×10^5 $eÅ^{-2}s^{-1}$.[3] Hence, the

STEM dose rate in this study was kept at the range ≤ 8.5×10^5 eÅ^{-2}s^{-1}. Dose tests for STEM-EDX and STEM/SEM-CL experiments are presented in Supplementary Figures 4, 5, 6 and 7, showing that the dose rate and doses chosen in this study caused neither structural changes nor Br desorption in spin-coated $CsPbBr_3$ materials.

STEM-EDX

The electron beam damage observed in $CsPbBr_3$ nano-thin films and nanocubes has often been attributed to the formation of pinholes caused by the desorption of Br species in earlier studies.[1,3] Dang et al. further corroborated this mechanism using STEM-EDX mapping, demonstrating a clear decrease in the intensity of the Br L signal with increasing electron dose.[3] To determine a dose threshold that minimizes Br loss from the $CsPbBr_3$ films fabricated by spin-coating in this study, we conducted a series of exposure tests on spin-coated $CsPbBr_3$ films by applying electron irradiation for a fixed duration of approximately 10 minutes. Supplementary Figure 4a shows that material loss was observed at a dose rate of 10^6 eÅ^{-2}s^{-1} and a total dose of 3000 eÅ^{-2}. A lower dose rate did not result in visible material loss (Supplementary Figure 4 b, c and d). To ensure that the electron beam effect is limited as much as possible, the low dose rate of 4×10^4 eÅ^{-2}s^{-1} (Supplementary Figure 4d) was chosen while maintaining adequate signal to noise ratio for characteristic peak detection for the EDX map shown in Supplementary Figure 5. EDX mapping at the dose rate presented in Supplementary Figure 5 did not result in a decrease in the intensity of the Br L signal, suggesting minimal Br desorption induced by electron beam.

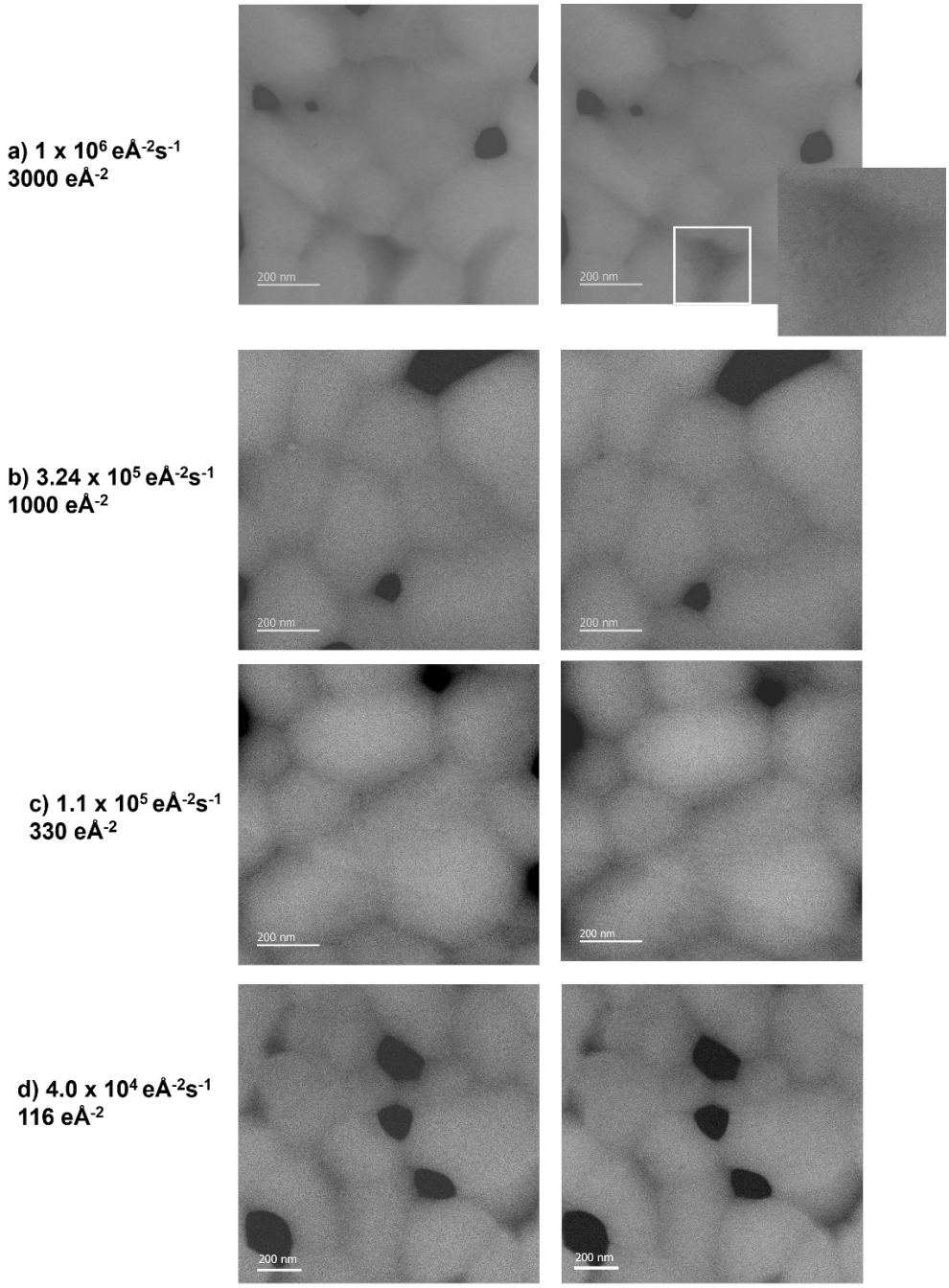

74

75 **Supplementary Figure 4: Dose exposure tests on spin-coated $CsPbBr_3$ films.** The film was

76 subjected to (a) 10^6 eÅ^{-2}s^{-1}, (b) 3.24 x 10^5 eÅ^{-2}s^{-1}, (c) 1.1 x 10^5 eÅ^{-2}s^{-1} and (d) 4.0 x 10^4 eÅ^{-2}s^{-1}

77 for a fixed duration of 10 minutes.

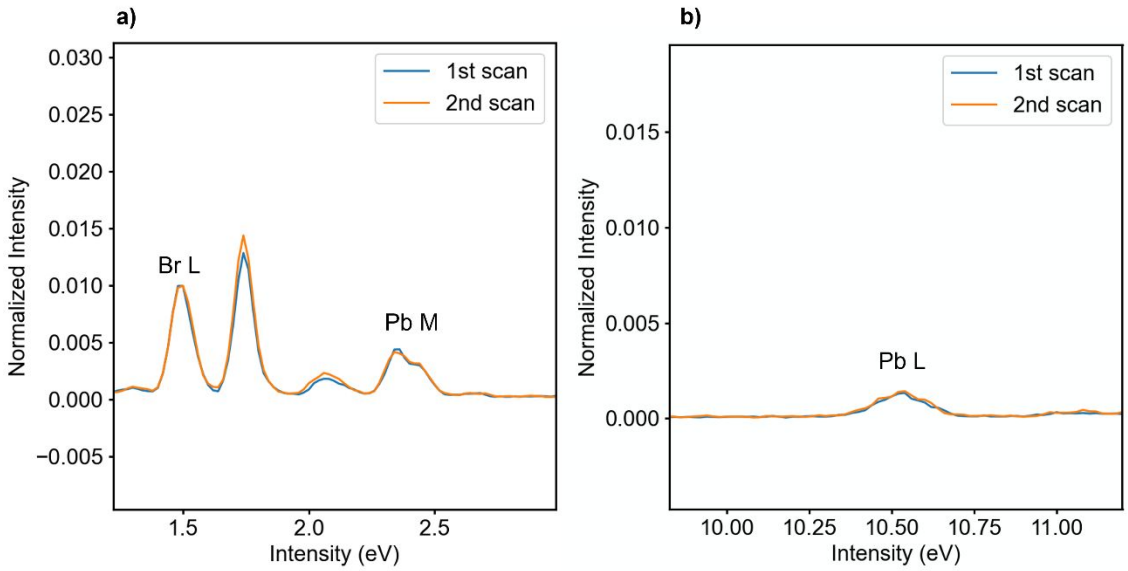

Supplementary Figure 5: EDX spectra collected during the first 10-minute EDX scan (total dose = 116 eÅ^{-2}) as compared to the second 10-minute EDX scan (total dose = 232 eÅ^{-2}) performed at the same region. Regions showing (a) Br L peak together with Pb M peak and (b) Pb L peak are extracted from the two spectra.

SEM-CL

Repeated CL hyperspectral scans were performed at an area adjacent to the device to investigate the effect of electron beam exposure on the $CsPbBr_3$ film using a dose rate of 1944 eÅ^{-2}s^{-1} and a cumulative dose of 19.44 eÅ^{-2} for one hyperspectral scan (Methods). The intensity of the CL emission obtained by summing the CL spectra at each pixel across the hyperspectral maps reveals a small decrease between the first scan relative to the subsequent scans (Supplementary Figure 6). Nevertheless, no major peak shift was detected among the different scans.

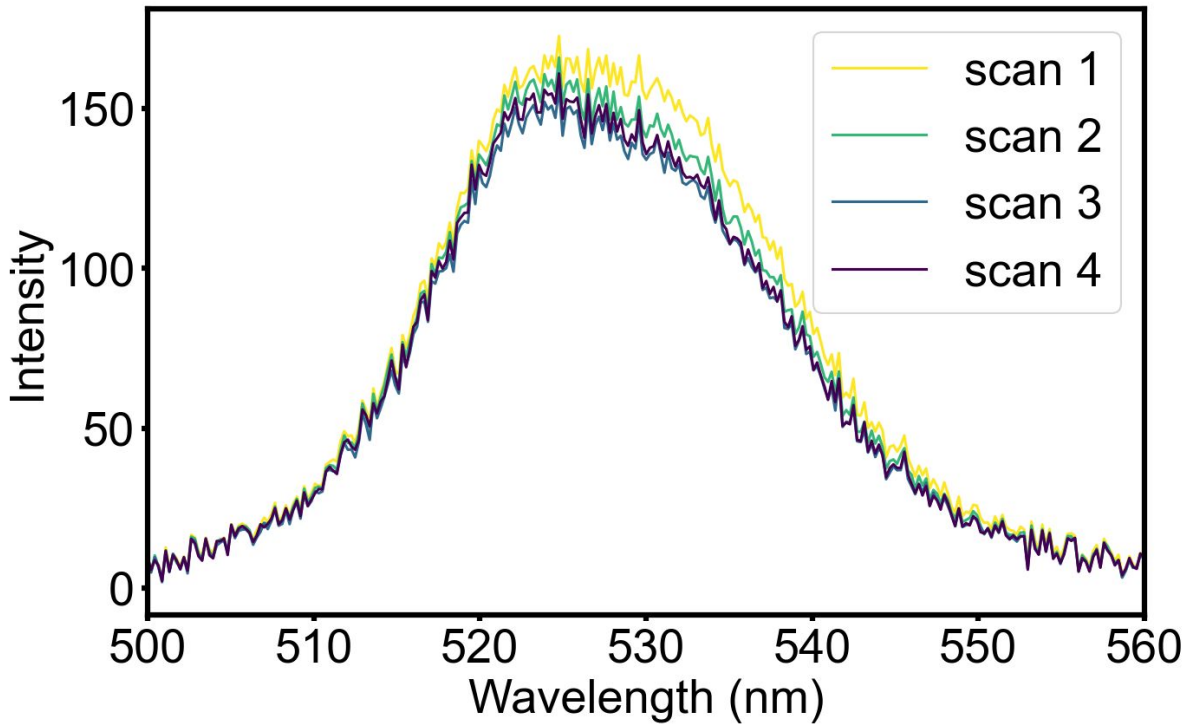

Supplementary Figure 6: SEM-CL dose study comparing the integrated CL spectra obtained from four consecutive CL hyperspectral scans. The integrated CL spectra were obtained from integrating the CL spectrum at each spatial pixel across the CL hyperspectral map.

STEM-CL

Multiple CL hyperspectral scans (22 $eÅ^{-2}$ per map, similar to the cumulative dose in SEM experiments, dose rate ~ 5.5×10^4 $eÅ^{-2}$) were performed on a region of $CsPbBr_3$ film on MEMs chips adjacent to the nano-LED device to investigate the effects of repeated electron exposure. The summed CL spectrum from the hyperspectral map showed a decrease in intensity after the first scan and remained constant for the subsequent three scans at an order of 10^6 (Supplementary Figure 7). The CL peak did not experience any visible peak shift (Supplementary Figure 7). STEM-CL induced a more pronounced reduction in CL intensity compared to SEM-CL, which is likely attributed to the higher electron beam energy used in

STEM (100 kV) relative to SEM (5 kV). The lower accelerating voltage in SEM reduces beam-induced damage, thereby better preserving the photophysical properties of the material. Nevertheless, STEM-CL can provide higher resolution than SEM due to the probe being more focused. This distinction highlights the complementary nature of the two techniques in evaluating CL behaviour.

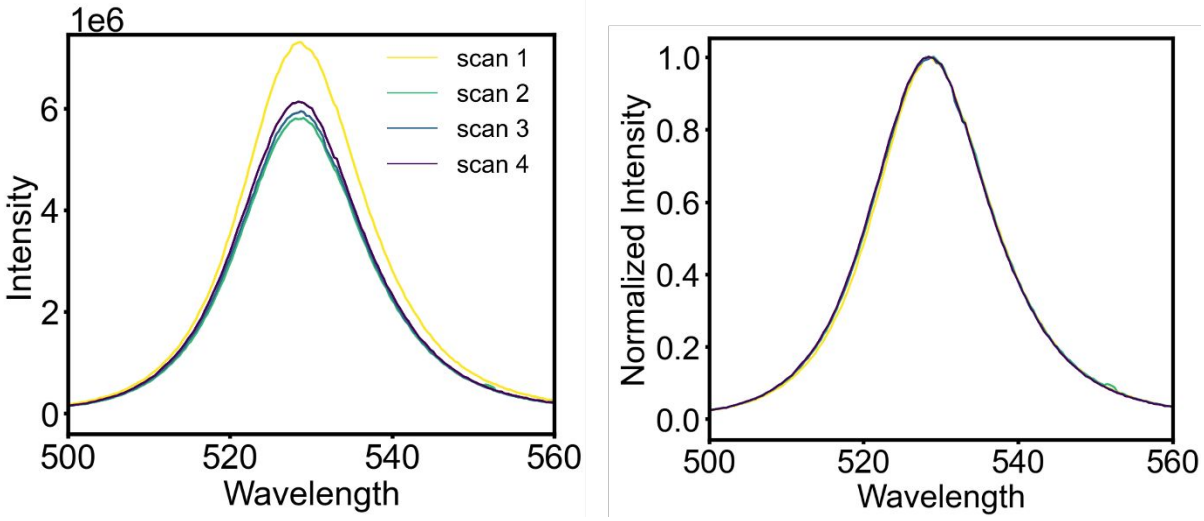

Supplementary Figure 7: STEM-CL dose study. CL spectra obtained by integrating the spectrum at each pixel within the CL hyperspectral map from the same region after four repeated scans (left) along with the corresponding spectra normalized to an intensity of 1 (right).

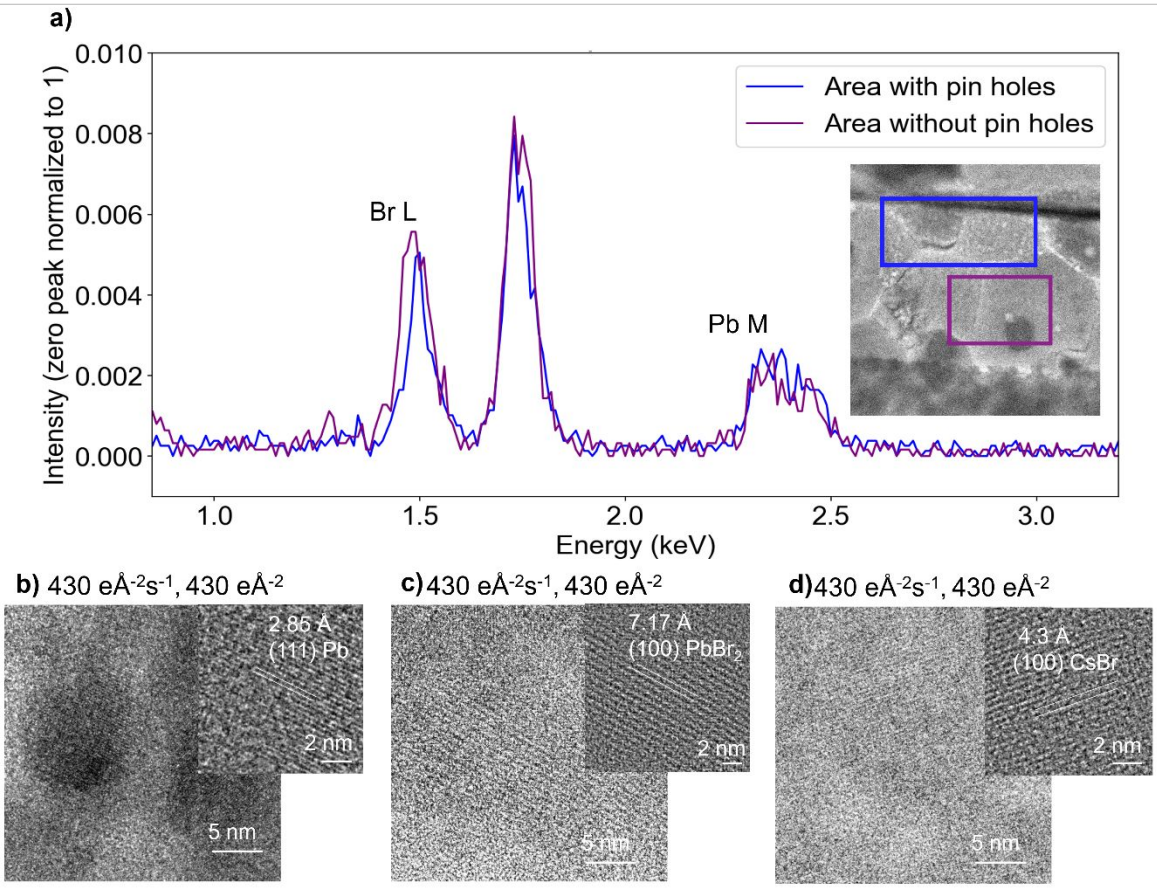

Supplementary Figure 8: (a) EDX spectra collected at the region shown in Figure 2b comparing areas with and without pin hole formation as marked in blue and purple respectively in the inset. BF-TEM images of various areas after 20 minutes of biasing, containing (b) high contrast Pb nanoparticles, (c) $PbBr_2$ and (d) CsBr together with a magnified insert showing the interplanar spacing.

Supplementary Table 1: EDX quantification of three areas with pin holes and three areas without pin holes

	Cs atomic %	Pb atomic %	Br atomic %
Area 1 (w/o pin holes)	19.3	20.1	60.6
Area 2 (w/o pin holes)	19.0	17.0	63.9
Area 3 (w/o pin holes)	19.9	20.1	60.0
Average	**19.4**	**19.1**	**61.5**
Area 4 (w pin holes)	24.0	20.6	55.5
Area 5 (w pin holes)	23.2	22.7	54.1
Area 6 (w pin holes)	24.4	20.0	55.6
Average	**23.9**	**21.1**	**55.0**

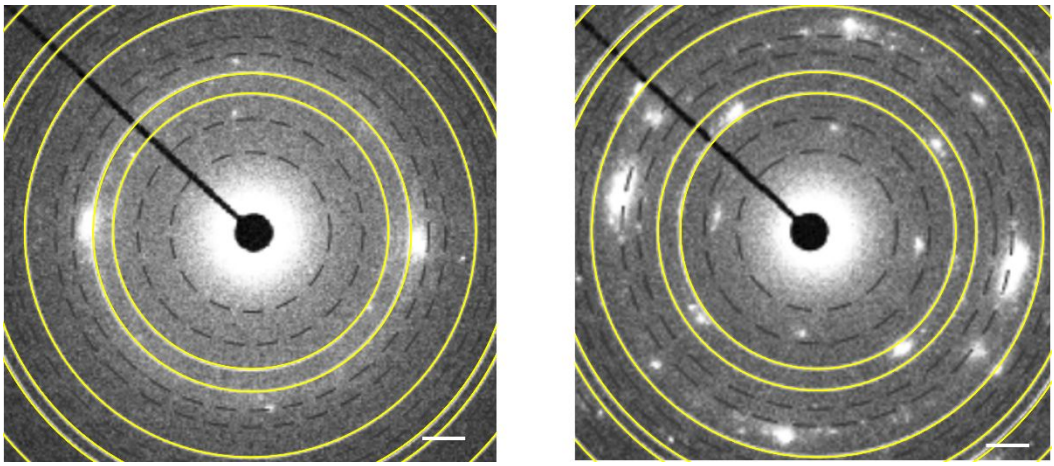

Supplementary Figure 9: An overlay of Cs^0 theoretical diffraction rings generated by CrystBox software (yellow = generated theoretical rings, dotted black = forbidden diffraction) with the experimental SAED patterns collected at two different areas. Scale bar = 1 1/nm.

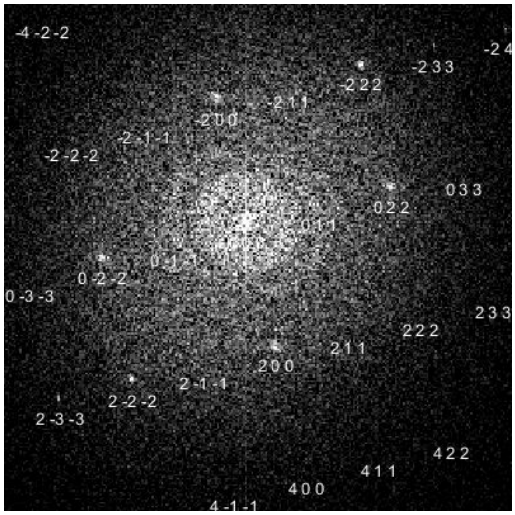

135

136 **Supplementary Figure 10: Diffractogram generated from HR-TEM image** at 0^{th} minute from

137 Figure 3 in the main manuscript fitted with a theoretical $CsPbBr_3$ pattern at the [0$\bar{1}$1] zone axis

138 simulated by CrystBox software.

139 ***In-situ* EL:**

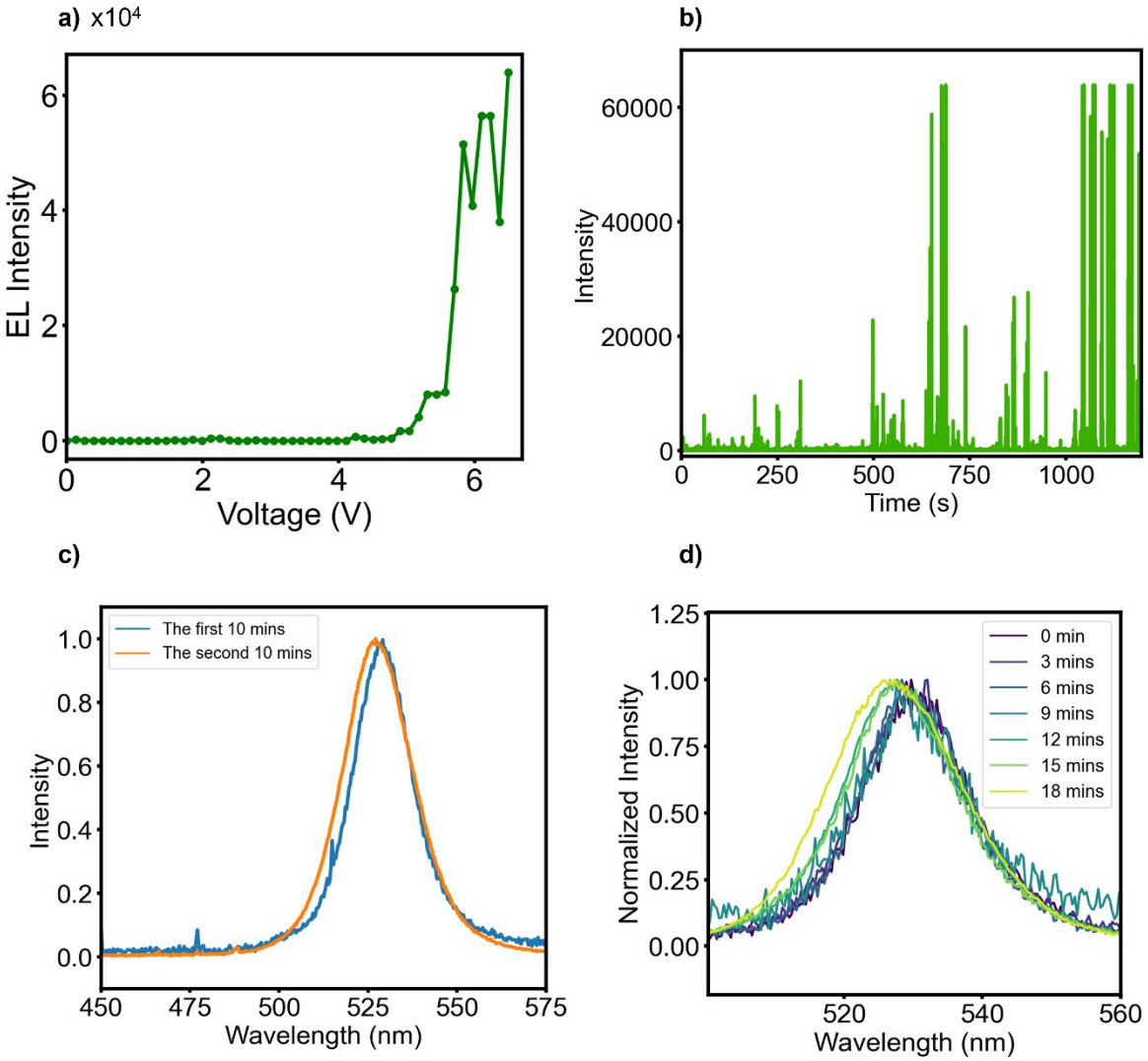

Supplementary Figure 11: EL tracking of the device biased with 14.5 V. (a) Temporal profile showing EL peak intensity with increasing voltage. (b) Temporal profile showing the EL peak intensity recorded every 0.12 s during a 20-minute bias application period. (c) A comparative plot of normalized EL intensity of the device collected during the first 10-minute and the second 10-minute bias showing 3-nm shift in EL peak after bias accompanied by a 4-nm increase in FWHM and (d) EL series of the devices during the 20-minute bias.

The intensity of the EL spectrum can be described as a function of temperature as expressed below:

$$\mathrm{I}(\hbar\omega) \propto \frac{1}{(e^{(E_0-\hbar\omega)/E_u})+1} \frac{(\hbar\omega)^3}{e^{(\hbar\omega t/k_B \mathrm{T})}} \quad (1)$$

whereby E_0 refers to the Urbach focus energy and E_u is the Urbach energy. $c, \hbar, \omega, k_B$ and T are the speed of light, the reduced Planck constant, the frequency of light, the Boltzmann constant and the temperature, respectively.[5-7] The Urbach energy (E_u) can be approximated as:

$$E_u = \frac{k_B \mathrm{T}}{\sigma_0} \quad (2)$$

in which σ_0 is the steepness parameter that can be determined experimentally.

From equation (1) and equation (2), the linewidth of EL and its relationship to temperature can be derived accordingly. A study conducted by Zhang et al. to investigate the linewidth (EL $_{\mathrm{FWHM}}$) and the Urbach energy (E_u) shows that EL $_{\mathrm{FWHM}} \approx 5.2\ E_u$ [3] (3). $\mathrm{EL}_{\mathrm{FWHM}}$ can be calculated in the unit of wavelength following the equation shown below:

$$\mathrm{EL}_{\mathrm{FWHM}} = hc\left(\frac{1}{\lambda_h} - \frac{1}{\lambda_l}\right) = \frac{hc\lambda_{FWHM}}{\lambda_h \lambda_l} \quad (4)$$

where h is the Planck constant. λ_H and λ_L are wavelengths marking the high energy and the lower energy part of the Full Width Half Maximum (FWHM) in the EL spectrum. Substituting the supplementary equations (2) and (4) into (3) yields equation (1) in the manuscript. In many cases, overestimation of temperatures was observed due to self-absorption effect. A scaling factor which varies between 0.911 and 0.995 is often incorporated to account for the effect and calibrate the initial temperature to the ambient temperature.[8]

Notably, EL exhibits blinking behaviour consistent with reports on devices comprising a small cluster of~ tens of $CsPbBr_3$ nanocrystals.[9] This behaviour likely arises because only a

limited number of nanocrystals are EL-active at a given time due to inefficient charge injection, dynamic electron-hole interactions and competing non-radiative recombination process.[9] In contrast, blinking is generally absent in large-area vertical devices where simultaneous emission from a large ensemble of nanocrystals produces stable averaged output.[9] The observation of nanoscale blinking as opposed to stable output in bulk devices highlights the need for nanoscale investigations to establish nanoscale design rules that translate into improved macroscopic device stability.

***In-situ* STEM-CL:**

An *in-situ* STEM-CL experiment on another nano-LED device at 6.5 V (the turn-on voltage region) was conducted. The STEM micrograph of the biased device (Supplementary Figure 12a) showed material loss at the SnO_2 interface, consistent with Figure 2 and 4 in the manuscript. From the results of the CL mapping (22 $eÅ^{-2}$ per map, dose rate ~ 5.5×10^4 $eÅ^{-2}s^{-1}$), the biased area generally exhibits a decrease in intensity of CL emission (Supplementary Figure 12b) and a shift in the fitted CL peak (Supplementary Figure 12c) as compared to the intensity recorded from the CL map of a pristine region different from the biased area (Supplementary Figure 12d, e, f and g). The CL peak averaged from the CL map of the biased area shows a 2 nm shift to lower wavelength (blue shift) as compared to the CL peak averaged from the map of the pristine region (Supplementary Figure 12g). Gaussian curve-fitting was carried out on each CL spectrum in each pixel of the CL map after PCA denoising (keeping 50 components). The blue shift was further confirmed by the histogram plotted in Supplementary Figure 12h. The EL emission did not exhibit a broadening effect that

is characteristic of temperature increase (Supplementary Figure 12i), suggesting that the blue shift in biased areas was primarily caused by biasing.

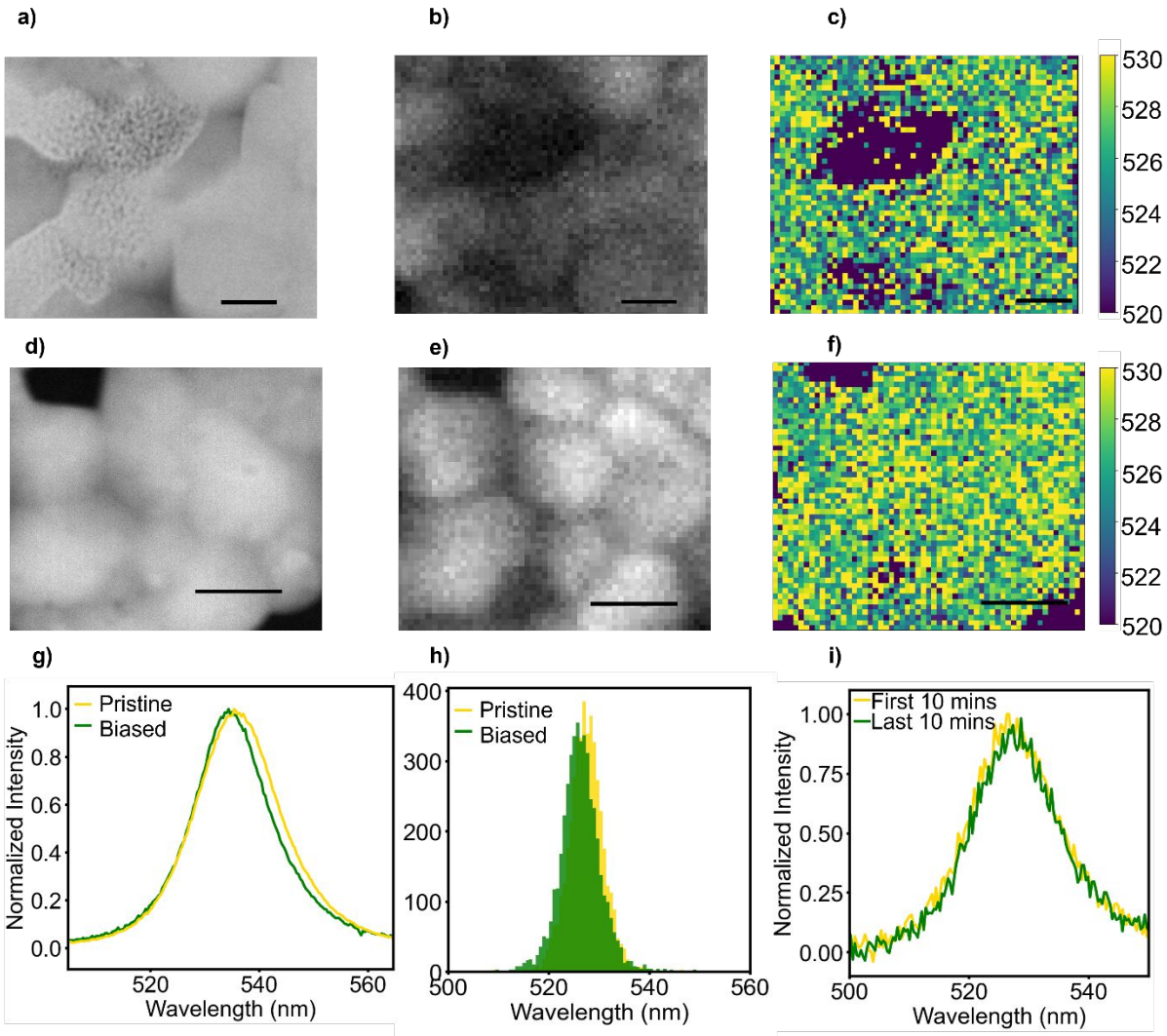

Supplementary Figure 12: *In-situ* STEM-CL biasing of another device at 6.5 V. (a) STEM image of a biased region together with (b) the corresponding hyperspectral CL map and (c) the distribution map of identified peaks from the fitted Gaussian curves on the hyperspectral map in juxtaposition with (d) STEM image of an adjacent pristine region and (e) the corresponding CL map and (f) the distribution of fitted peaks (Scale bar = 200 nm). (g) Averaged and Normalized CL emission spectra of a damaged region and a pristine region, with the damaged region exhibiting a 2-nm blue shift (Scale bar = 200 nm). (h) Histogram showing the

distribution of the peaks from the fitted Gaussian curves for the pristine region compared to the biased one. (i) Evolution of the EL peak energy during the first 10 minutes and the last 10 minutes of constant 6.5 V application.

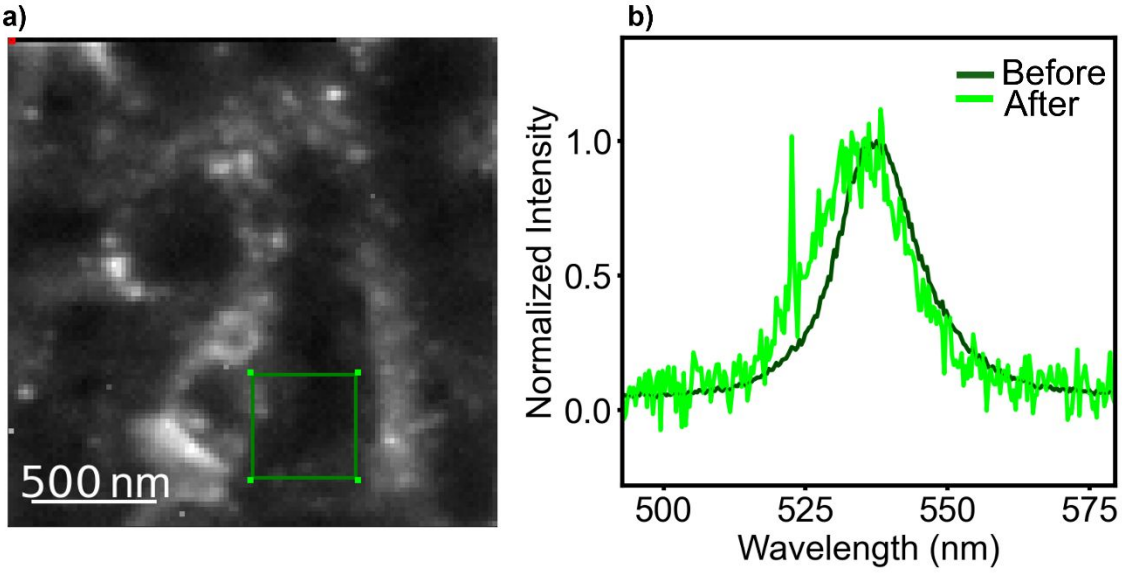

Supplementary Figure 13: Comparison of the CL activity of the region with high defect density before and after bias. (a) CL map of the device before bias with the area possessing elevated defect density marked in green (as identified in the manuscript). (b) Comparative plot of normalized CL spectra of the region marked in green in (a) before and after bias, indicating a 2-nm blue shift after bias.

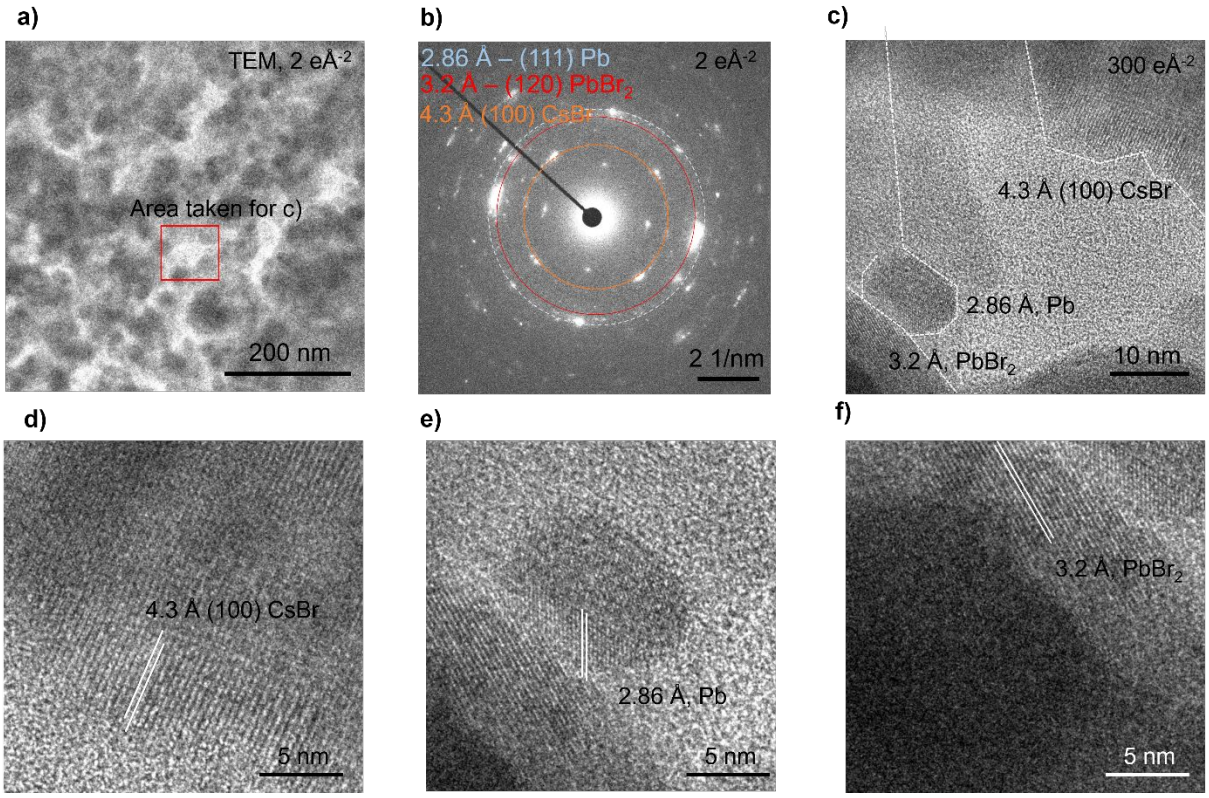

Supplementary Figure 14: HR TEM of damaged regions under application of 14.5 V. (a) HR-TEM image of a damaged area showing pin-hole formation with (b) the corresponding SAED pattern. (c) Magnified view of the area highlighted in red in (a) together with images showing the calculated interplanar spacing of (d) CsBr, (e) Pb and (f) $PbBr_2$ found in (c).

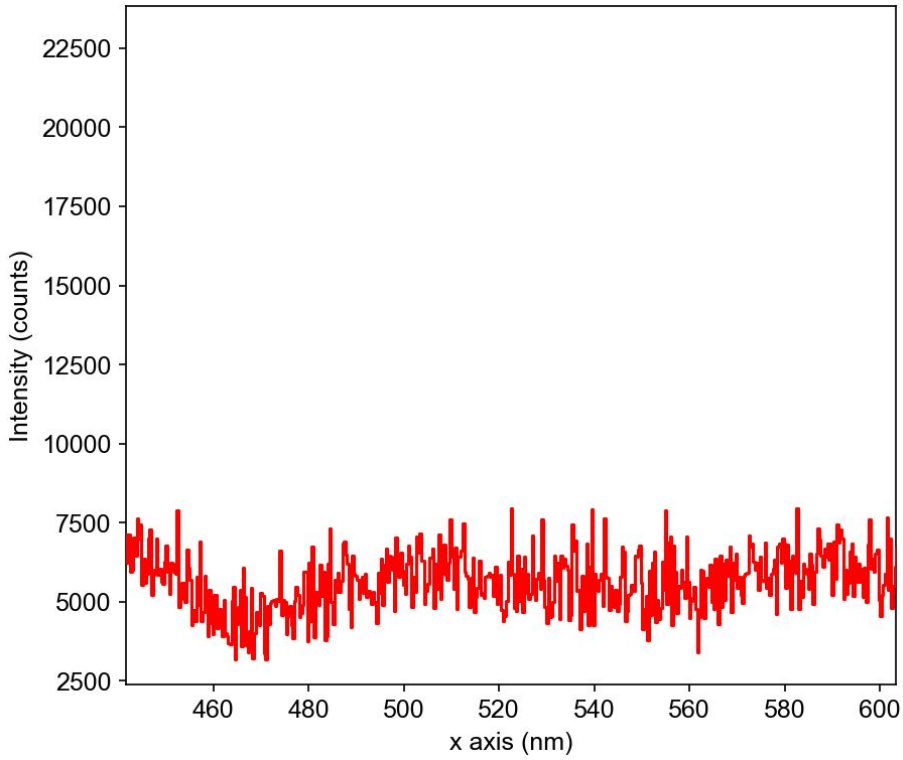

Supplementary Figure 15: CL spectrum of $PbBr_2$ deposited film on a MEMs chip under similar imaging conditions to the $CsPbBr_3$ deposited film at room temperature. The spectrum generated from a 2 µm × 2 µm area of $PbBr_2$ deposited film did not show emission at 475 nm as expected from $PbBr_2$ under UV-Vis and Fluorescence spectra in a previous study.[10]

Reversible biasing:

A SEM-CL experiment was conducted on a nano-LED device with a turn-on voltage of 5 V (Supplementary Figure 16). After one minute of forward +5 V biasing, the biasing was stopped for CL map acquisition. The device exhibited a reduction in CL intensity, implying formation of defects which act as traps for non-radiative recombination (Supplementary Figure 16b). The device was subjected to reverse biasing of -5 V for one minute. The CL spectra collected after completion of reverse biasing showed an increase in peak intensity, indicating that defect generation induced by forward biasing was reversed by reverse biasing.

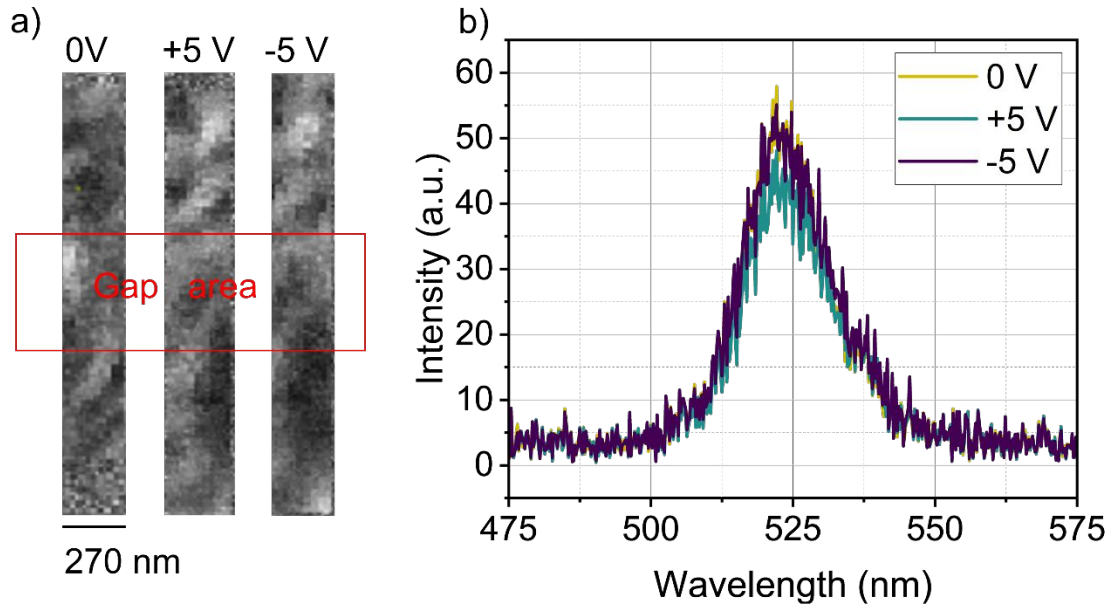

231

232 **Supplementary Figure 16: *In-situ* SEM-CL experiment on a nano-LED under +5 V forward**

233 **biasing followed by -5 V reverse biasing**. (a) CL hyperspectral maps of the areas collected

234 before bias (0 V), after 1 minute of +5 V biasing and after 1 minute of -5 V biasing. (b) CL

235 spectra of the regions between the electrodes.

236

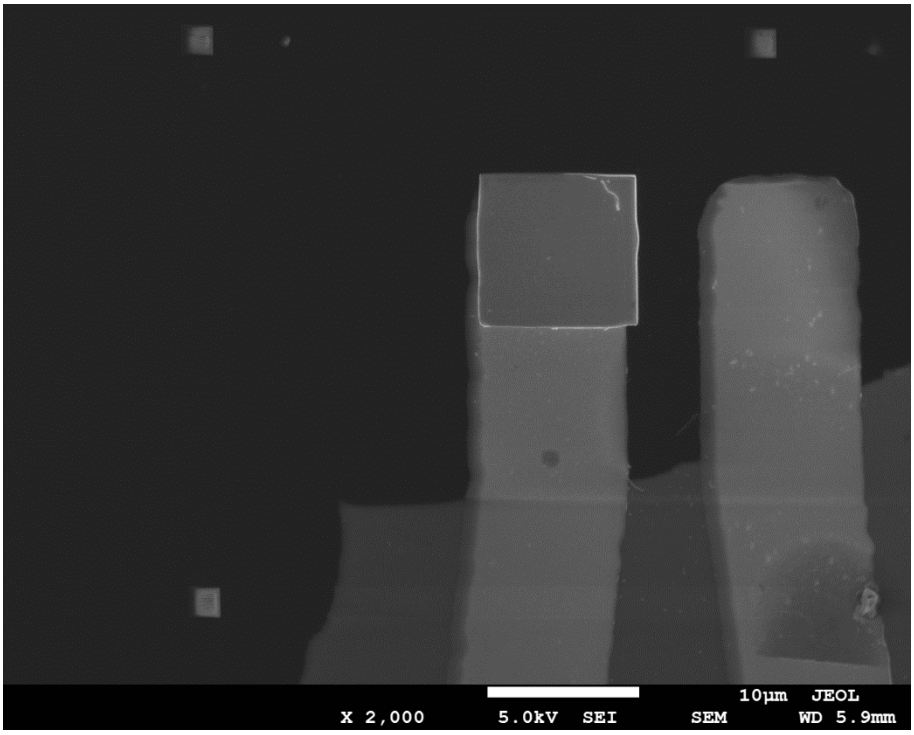

Supplementary Figure 17: SEM image of the first sputtered layer. The first ITO layer was deposited together with three alignment marks at the top-left, top-right and bottom-left corners for fine alignment of subsequent layers relative to the first layer.

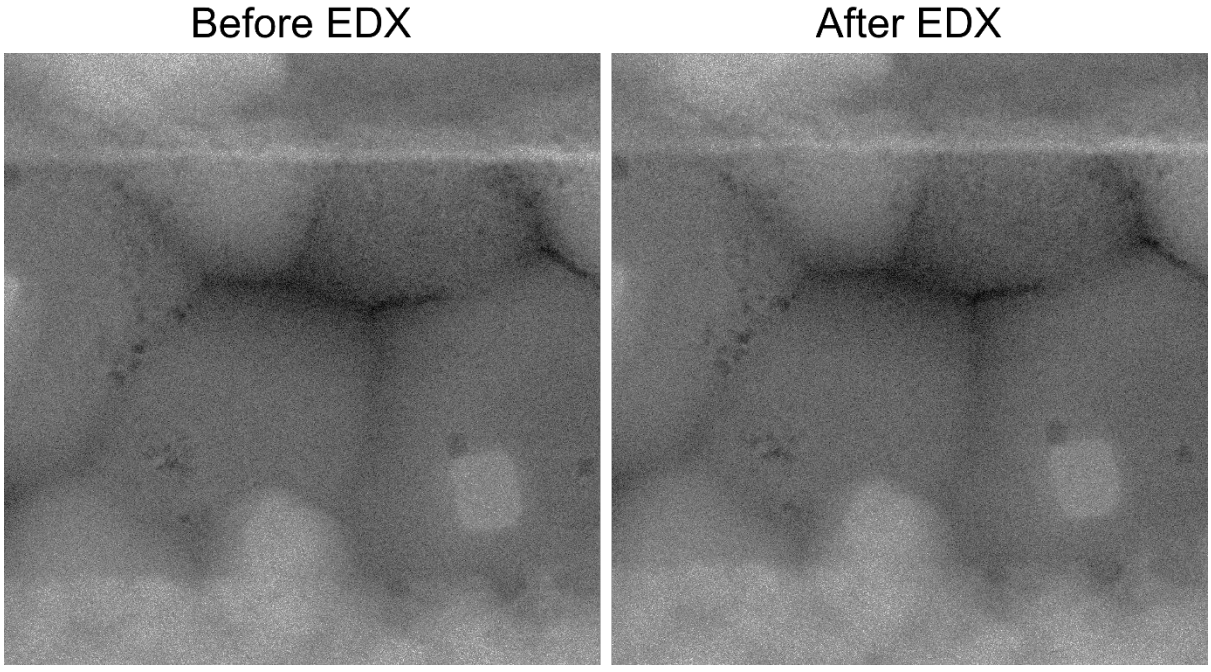

Supplementary Figure 18: STEM images captured before and after EDX mapping.

243 REFERENCES

244 1 Diao, F.; Zhang, Q.; Wang, J.; Liang, W.; Rosei, F.; Xue, X.; Wang, Y. Thickness-
245 Dependent Microstructural Evolution Of $CsPbBr_3$ Nanobricks Induced by Electron Beam
246 Irradiation. *Small Structures*. **2024**, 5, 2300577.
247 https://doi.org:https://doi.org/10.1002/sstr.202300577

248 2 Dang, Z.; Shamsi, J.; Akkerman, Q. A.; Imran, M.; Bertoni, G.; Brescia, R.; Manna, L.
249 Low-Temperature Electron Beam-Induced Transformations Of Cesium Lead Halide
250 Perovskite Nanocrystals. *ACS Omega*. **2017**, 2, 5660-5665.
251 https://doi.org:10.1021/acsomega.7b01009

252 3 Dang, Z.; Shamsi, J.; Palazon, F.; Imran, M.; Akkerman, Q. A.; Park, S.; Bertoni, G.;
253 Prato, M.; Brescia, R.; Manna, L. In Situ Transmission Electron Microscopy Study Of Electron
254 Beam-Induced Transformations In Colloidal Cesium Lead Halide Perovskite Nanocrystals.
255 *ACS Nano*. **2017**, 11, 2124-2132. https://doi.org:10.1021/acsnano.6b08324

256 4 Huang, D.; Xie, P.; Pan, Z.; Rao, H.; Zhong, X. One-Step Solution Deposition Of
257 $CsPbBr_3$ Based On Precursor Engineering For Efficient All-Inorganic Perovskite Solar Cells.
258 *Journal of Materials Chemistry A*. **2019**, 7, 22420-22428.
259 https://doi.org:10.1039/C9TA08465G

260 5 Zhang, G.; Ren, Z.; Yuan, Y.; Xing, S.; Zhao, B.; Zou, C.; Di, D. Temperature
261 Characterization Of Perovskite LEDs By Electroluminescence. *Nano Letters*. **2025**, 25, 177-
262 183. https://doi.org:10.1021/acs.nanolett.4c04676

263 6 Wurfel, P. The Chemical Potential Of Radiation. *Journal of Physics C: Solid State*
264 *Physics*. **1982**, 15, 3967. https://doi.org:10.1088/0022-3719/15/18/012

7 Daub, E.; Würfel, P. Ultralow Values Of The Absorption Coefficient Of Si Obtained from Luminescence. *Physical Review Letters*. **1995**, 74, 1020-1023. https://doi.org:10.1103/PhysRevLett.74.1020

8 Schötz, K.; Askar, A. M.; Köhler, A.; Shankar, K.; Panzer, F. Investigating The Tetragonal-To-Orthorhombic Phase Transition Of Methylammonium Lead Iodide Single Crystals By Detailed Photoluminescence Analysis. *Advanced Optical Materials*. **2020**, 8, 2000455. https://doi.org:https://doi.org/10.1002/adom.202000455

9 Sharma, D. K.; Hirata, S.; Vacha, M. Single-Particle Electroluminescence of CsPbBr3 Perovskite Nanocrystals Reveals Particle-Selective Recombination and Blinking as Key Efficiency Factors. Nat. Commun. **2019**, 10 (1), 4499. https://doi.org/10.1038/s41467-019-12512-y.

10 Tawil, C. A.; Kurdi, R. E.; Patra, D. Cesium Lead Bromide Perovskites: Synthesis, Stability, And Photoluminescence Quantum Yield Enhancement By Hexadecyltrimethylammonium Bromide Doping. *ACS Omega* **7**. **2022**, 20872-20880. https://doi.org:10.1021/acsomega.2c01490